Research Square

Preprints are preliminary reports that have not undergone peer review.
They should not be considered conclusive, used to inform clinical practice,
or referenced by the media as validated information.

Multi-scale characterization of preferential contaminant transport pathways in the Igbeti marble mining environment in southwestern Nigeria: Integrating VES, XRD, and SEM-EDS analyses

Ayodele Christianah Adeboye

24-68em003pg@students.unilorin.edu.ng

University of Ilorin

Oladele Ajiboro Omotoso

University of Ilorin

Omolayo Ajoke Omorinoye

University of Ilorin

Research Article

Keywords: Groundwater vulnerability, Marble mining, Hydrogeophysics, Aquifer protective capacity, Rock-fluid interaction, Basement complex

Posted Date: October 30th, 2026

DOI: https://doi.org/10.21203/rs.3.rs-11252381/v1

License: This work is licensed under a Creative Commons Attribution 4.0 International License. Read Full License

Additional Declarations: No competing interests reported.

Abstract

Mining activities in fractured basement terrains pose severe groundwater contamination risks, yet the precise micro-hydrogeological mechanisms governing contaminant migration remain poorly understood due to the inherent non-uniqueness of standalone geophysical interpretations. This study develops a multi-scale conceptual model of groundwater vulnerability in the Igbeti marble mining district, Nigeria, by integrating macro-scale Vertical Electrical Sounding (VES), meso-scale X-ray Diffraction (XRD), and micro-scale Scanning Electron Microscopy with Energy Dispersive X-ray Spectroscopy (SEM-EDS). The geophysical vulnerability assessment revealed uniformly extremely high aquifer vulnerability and poor protective capacity across the study area, driven by thin overburden (0.3–3.6 m) and highly fractured media, yielding exceptionally low longitudinal conductance values (S = 0.004–0.427 mhos). Ground-truthing these anomalies with XRD and SEM-EDS demonstrated that this vulnerability is fundamentally rooted in the intrinsic lithological and mineralogical properties of the basement complex. The aquifer matrix is predominantly composed of highly resistive, unweathered quartz (e.g., 62.63 wt% in TSRK1) and feldspars, exhibiting advanced chemical leaching and a distinct lack of protective, high-cation-exchange-capacity clay layers. Furthermore, while localized carbonate-rich zones (70.74 wt% dolomite in ARK1) provide some geochemical buffering, the dominant quartz-rich zones lack neutralizing capacity, facilitating the rapid mobilization of acidic leachates and heavy metals. These findings confirm that the fractured silicate and carbonate aquifers offer negligible natural attenuation to mining leachates. Consequently, mitigating groundwater contamination in this and similar mining environments requires moving beyond passive reliance on natural attenuation to implementing strict, science-based buffer zones, engineered impermeable tailings dams, and continuous hydrogeochemical monitoring to safeguard regional water resources.

1 Introduction

The escalating demand for industrial minerals has driven a surge in mining activities globally, particularly in developing nations where regulatory frameworks and environmental monitoring often lag behind extraction rates [1, 2] While mining operations are critical for economic development, they profoundly alter local hydrogeological systems and introduce severe contamination risks. The excavation of bedrock, coupled with the indiscriminate disposal of mine tailings and the use of heavy machinery, generates acidic leachates and mobilizes heavy metals. These contaminants frequently infiltrate shallow aquifer systems, posing a severe threat to groundwater quality, which serves as the primary potable water source for many rural and semi-urban communities [3, 4].

In Southwestern Nigeria, the Igbeti district represents a critical hotspot for such environmental vulnerability. Recognized as a major hub for marble and limestone mining, the area is characterized by extensive open-pit excavations and unengineered waste dumpsites [5–7]. The local hydrogeology is dominated by fractured carbonate bedrock and thin overlying weathered profiles [8–10]. In such heterogeneous, fractured media, groundwater flow and contaminant transport are highly channelized through preferential pathways. Consequently, the rapid infiltration of mining leachates into these fractured aquifers bypasses the natural attenuation capacity of the vadose zone, leading to the swift degradation of groundwater quality. Despite the recognized environmental threat, the precise micro-hydrogeological mechanisms governing contaminant migration, and the specific rock-fluid interactions occurring within these fractured marble aquifers, remain poorly understood.

Traditionally, groundwater contamination studies in similar geological settings have relied heavily on either point-source hydrogeochemical sampling or surface geophysical methods. While hydrogeochemistry provides precise fluid composition, it is inherently limited by its spatial resolution, offering only localized "snapshots" of

contamination [11]. Conversely, geoelectrical methods, particularly Vertical Electrical Sounding (VES) and Electrical Resistivity Tomography (ERT), are widely deployed to map subsurface architecture and delineate contaminant plumes based on resistivity contrasts [12, 13]. However, geophysical interpretations suffer from the fundamental problem of "non-uniqueness" [14]. For instance, a low-resistivity anomaly mapped by VES could represent a saline contaminant plume, a conductive clay-rich weathered zone, or simply a water-saturated fracture. Without ground-truthing, distinguishing between lithological controls and actual fluid contamination remains highly speculative [15].

To bridge these knowledge gaps, recent advancements in environmental geosciences advocate for a multi-modal, multi-scale approach that couples macro-scale geophysics with meso- and micro-scale mineralogical analyses [16, 17]. Integrating VES with X-ray Diffraction (XRD) and Scanning Electron Microscopy equipped with Energy Dispersive X-ray Spectroscopy (SEM-EDS) provides a comprehensive framework to calibrate geophysical models. While VES defines the physical architecture and spatial extent of the contamination plumes, XRD identifies the bulk mineralogical composition that governs the baseline resistivity and geochemical reactivity of the aquifer matrix. Crucially, SEM-EDS operates at the micro-scale to reveal the actual morphological and chemical pathways of contaminant transport—such as mineral dissolution features, fracture linings, and secondary precipitates—that dictate how the rock matrix interacts with and attenuates the migrating leachate [18, 19].

Despite the proven efficacy of these techniques in isolated applications, their integrated application to understand rock-fluid interactions in carbonate-dominated mining environments remains rare. Therefore, this study aims to develop a multi-scale conceptual model of groundwater contamination in the Igbeti marble mining area. The specific objectives are to: (1) map the subsurface hydrogeological architecture and delineate contaminant plumes using VES; (2) determine the bulk mineralogical composition via XRD to constrain the lithological influences on geophysical resistivity; and (3) investigate the micro-morphological and elemental alterations using SEM-EDS to elucidate the micro-scale mechanisms of rock-fluid interaction and preferential contaminant transport. Ultimately, this integrated approach will provide a robust, mechanistic understanding of groundwater vulnerability in fractured mining environments.

2 Materials and method

2.1 Study area and geological Setting

The study area is situated within the geographic coordinates of latitudes 8° 35' 54.20" N to 8° 50' 45.27" N and longitudes 3° 59' 27.02" E to 4° 12' 43.34" E, covering an approximate area of 667 km² (Fig. 1). The region lies within the Olorunsogo Local Government Area of Oyo State, Nigeria, encompassing major settlements such as Igbeti, Alaguntan, Tesi, and Igbori.The area is drained by a dendritic drainage network critical for local agriculture and the domestic water supply. Geologically, the area is underlain by lithologies of the Pan-African Older Granite Series, Meta-Sedimentary Series, Migmatite-Gneiss Complex, and Cataclastic Rocks [20, 10]. The Meta-Sedimentary Series, trending NNE-SSW, is represented by amphibole schist, amphibolite, and the prominent marble deposits for which Igbeti is renowned. Cataclastic rocks, including silicified and sheared rocks with large quartz veins, are similarly oriented and associated with regional fault zones, while the Migmatite-Gneiss Complex dominates the southeastern portion of the study area.

2.2 Multi-scalar methodological framework

To overcome the inherent non-uniqueness of standalone geophysical interpretations in heterogeneous fractured bedrock, this study employs a multi-faceted, multi-scalar approach. Knowledge gaps frequently exist when interpreting geochemical, geological, and hydrological data in fractured environments where subsurface characteristics change abruptly. Minimally invasive geophysical methods bridge the spatial gap of sparse borehole locations by producing spatially extensive data to map groundwater flow and contaminant fate [11]. By coupling these geophysical techniques with targeted geochemical and mineralogical characterization, this research identifies difficult-to-locate preferential contaminant transport pathways, saving time and resources by focusing on primary transport zones [16, 17].

2.3 Macro-scale geophysical mapping

Vertical Electrical Sounding (VES) was conducted to investigate subsurface resistivity characteristics. In resistivity measurement, electric current is introduced into the subsurface via a pair of current electrodes (C1 and C2), while the resulting potential difference is recorded by an internal pair of potential electrodes (P1 and P2). The relationship between the measured resistance ($R = V/I$) and the sensor layout is represented by a geometry factor (K), yielding the apparent resistivity (ρa) of the heterogeneous medium. The Schlumberger array was specifically selected for this investigation due to its superior sensitivity to vertical resistivity variations, greater depth penetration, and operational efficiency compared to the Wenner array [21]. In this configuration, the spacing of the outer current electrodes is systematically varied, while the inner potential electrodes remain relatively constant, only being expanded when the measured voltage becomes too small to resolve accurately.

A total of thirty (30) VES stations were occupied across Igbeti (10), Tesi (10), Igbori (5), and Alaguntan (5). Stations were aligned along collinear profiles (Fig. 2) to facilitate the two- dimensional description of geoelectric thickness and resistivity distribution. A maximum current electrode half-spacing (AB/2) of 100 m was employed to ensure adequate depth penetration into the weathered and fractured basement units. Field measurements were acquired using a Terrameter, and the apparent resistivity data were processed and inverted using DIPRO™ software. The inversion algorithm discretized the subsurface into rectangular blocks, applying a finite-difference optimization technique to estimate true resistivity values and layer thicknesses [22, 23], enabling the delineation of subsurface lithological layers and fractured zones.

2.4 Meso-scale mineralogical baseline

To evaluate the mineralogical composition and its implications on the resistivity patterns revealed by the geophysical models, representative bulk rock and weathered profile samples (e.g., TSRK1, TSRK2, IRK1, ARK1) were collected from zones corresponding to VES anomalies. Approximately 1–3 g of each field sample was oven-dried and pulverized to a fine powder (< 75 µm). Powder X-ray diffraction (XRD) analyses were conducted using a Bruker D8 Advance powder diffractometer equipped with a LynxEye detector and a Cu Kα X-ray source (λ = 1.54 Å) at the X-ray Crystallographic Center, University of Maryland, College Park, USA. Continuous θ–2θ scans were collected over a 2θ range of 5–90° with a step size of 0.02° and a scan rate of 5.6×10^{-4} ° s^{-1}. Crucially, mirror optics were utilized to reduce errors in peak positioning caused by any diffracting surface displacement. Mineral phase identification and initial semi-quantitative screening were performed using QualX software [24], cross-referenced with the International Centre for Diffraction Data (ICDD) PDF database and the Crystallography Open Database (COD). Subsequently, rigorous quantitative mineralogical analysis was conducted using Full Pattern Summation (FPS) via the powdR package in R [25]. Reference patterns were sourced from the comprehensive RockJock library [26]. Phase concentrations were computed by optimizing the scaling factors of the selected

reference patterns to fit the measured diffractograms (restricted to 10–80° 2θ to minimize high-angle background noise), utilizing Reference Intensity Ratios (RIR). Phase concentrations were calculated assuming a closed sum of 100% for the identified crystalline phases. Based on the derived weight percentages, minerals were classified as major (> 50%), secondary (10–30%), and minor (5–10%) phases. This integrated two-step approach allowed for the precise determination of primary resistive minerals (e.g., quartz, feldspars) versus secondary conductive phases (e.g., clays, amphiboles, carbonates), providing a direct petrophysical link to the observed geoelectrical anomalies.

2.5 Micro-scale morphological and elemental analysis

To interrogate small-scale morphological differences and elemental signatures within the fracture networks, selected undisturbed rock samples were examined using Scanning Electron Microscopy coupled with Energy Dispersive X-ray Spectroscopy (SEM-EDS). Analyses were performed using a SU-70 field-emission scanning electron microscope (Hitachi High-Technologies) at the NanoCenter AIM Lab, University of Maryland, College Park, USA. Samples were mounted on aluminum stubs using carbon tape, which helped secure the powder in place and enhance electrical conductivity during imaging, and were then sputter-coated with a 2 nm-thick conductive layer of gold/palladium to minimize charging. The prepared samples were examined using SEM in secondary electron mode at accelerating voltages ranging from 5 to 15 kV and working distances of 14.9–15.1 mm. High-resolution micrographs were acquired to identify micro-morphological features such as mineral dissolution pits and secondary fracture coatings. Concurrently, EDS point analyses (four distinct points per sample) were conducted to determine the elemental weight percentages (wt%) of these coatings. This targeted approach specifically identifies aluminosilicate (clay) and siliceous signatures, while explicitly excluding Au and Pd coating artifacts from geochemical interpretations.

2.6 Aquifer vulnerability assessment

To assess the protective capacity of the overburden, the Dar-Zarrouk parameters and the Aquifer Vulnerability Index (AVI) were computed for each VES point based on the interpreted layer parameters. The longitudinal unit conductance (S) quantifies the electrical conductance of the protective layers above the principal aquifer, while the AVI defines vulnerability in terms of the hydraulic resistance (c) of the overburden. To estimate hydraulic conductivity (K) from resistivity, an empirical relationship was applied [27], linking low resistivity to clay-rich materials with high protective capacity. The mathematical formulations for all geophysical and vulnerability parameters are summarized in Table 1.

Table 1
Mathematical Formulations for Geophysical and Vulnerability Parameters

Parameter	Equation	Description of Variables
Apparent resistivity (ρ_a) [28]	ρ_a = K × R = K × (V / I)	V = Voltage, I = Current, K = Geometry factor of the electrode array.
Longitudinal unit conductance (S) [29]	S = Σ (h_i / ρ_i) *(for i = 1 to n)*	h_i = Thickness (m), ρ_i = Resistivity (ohm-m) of the *i-th* protective layer.
Hydraulic conductivity (K) [27]	K (m/s) = 0.975 × 10^{-5} × $\rho^{-1.195}$ K (m/d) = K (m/s) × 86,400	ρ = Layer resistivity (ohm-m).
Hydraulic resistance (c) [30]	c = Σ (h_i / K_i) *(for i = 1 to n)*	h_i = Thickness (m), K_i = Hydraulic conductivity (m/d) of the i-th layer.
Transverse unit resistance (T) [29]	T = Σ (h_i × ρ_i) *(for i = 1 to n)*	Represents the resistance to horizontal flow in the protective layers.
Coefficient of anisotropy (λ) [29]	λ = $\sqrt{(\mathrm{T}/\mathrm{S})}$	Provides insight into the heterogeneity of the overburden sequence.

3 Results

3.1 Qualitative description of geoelectric curves

Table 2 presents the thickness and apparent resistivity of geoelectric layers estimated through the inversion of vertical electrical sounding (VES) data across the study area. The typical curve types derived from the apparent resistivity versus electrode spacing (AB/2) plots, along with their distributions, are presented in Fig. 3, revealing distinct subsurface patterns. The Tesi area is characterized by predominantly ascending resistivity profiles, with curve types dominated by A- and K-related variants (3 AA, 3 AK, 3 AKQ, and 1 KQH). In contrast, the Igbori area exhibits the greatest diversity of curve types (QHK, QH, OH, BA, and HA), each represented by a single occurrence, corresponding to complex subsurface layering. The Igbeti area shows a strong predominance of H- and K-combination curves (3 HK, 3 KQ, 2 HA, 1 KH, and 1 KHA), representing intermediate low-resistivity layers sandwiched between more resistive materials. Similarly, the Alaguntan area is dominated by K-H-A variants (2 KH, 2 KHA, and 1 HK), corresponding to subsurface profiles containing fractured, clayey, or transitional zones. Curve types featuring H-components, which are common in Igbeti and Alaguntan, represent conductive, low-resistivity overburden layers that contribute to the longitudinal conductance (S) and hydraulic resistance (C) of the protective overburden. Conversely, the A-dominated profiles in Tesi correspond to more resistive overburden sequences.

3.2 Quantitative description of geoelectric cross-sections

The geoelectric cross-sections (Fig. 4a–d) reveal a multi-layered subsurface with significant lateral variations, generally comprising a thin topsoil, a weathered basement (principal aquifer), and an underlying fractured to fresh basement. Across the 1800 m profiles at Tesi and Igbeti, and the 800 m profiles at Igbori and Alaguntan, the topsoil remains thin (0.3–3.6 m) with resistivity values of 7–506 Ωm, corresponding to clayey to lateritic soils. Beneath this, the weathered basement spans depths of 2 to 55 m. In Tesi, this zone exhibits resistivity values of 46–1,586 Ωm, transitioning into a fractured basement (5–40 m deep, 249–3,889 Ωm) where moderate values (300–1,200 Ωm) correspond to saturated fractures, and higher values (> 2,000 Ωm) denote less fractured rock. Similarly, the Igbeti profile displays a weathered basement (140–1,830 Ωm), with lower resistivity zones (140–456 Ωm) corresponding to saturated materials, underlain by a fractured to fresh basement (> 504 Ωm) representing competent bedrock.

Table 2
VES inversion results

VES	Location	h_1 (m)	h_2 (m)	h_3 (m)	h_4 (m)	ρ_1 (Ωm)	ρ_2 (Ωm)	ρ_3 (Ωm)	ρ_4 (Ωm)	ρ_5 (Ωm)
1	Tesi	2.8	6.1	6.6	17.2	77.4	972.8	444.9	273.8	20381.6
2	Tesi	0.3	10.3	17.3	–	64.8	285.9	483.4	160.6	–
3	Tesi	2.3	4.8	22.4	–	505.6	1585.5	3888.5	318.9	–
4	Tesi	0.4	1.2	13.7	25.6	6.8	456.8	2030	3196.6	2956.3
5	Tesi	0.9	10.8	25.2	–	179.5	320.9	503.5	687	–
6	Tesi	0.4	4.8	2.8	–	14.8	45.7	248.9	19387.5	–
7	Tesi	0.9	1.7	26.2	39	35.9	247.4	1190.7	1170.8	827.5
8	Tesi	0.7	3.4	27	19.2	22.7	551	1762.5	720.7	447.6
9	Tesi	0.5	9.3	13.3	–	54.1	393.9	877.8	1048.7	–
10	Tesi	1.7	11.8	30.4	–	111.3	159.7	944.8	1026.2	–
1	Igbori	0.5	3.2	25	18.8	1865.3	599	117.2	209.4	167.5
2	Igbori	1.4	6.6	28.8	–	1152.9	731.2	223.6	293	–
3	Igbori	4.8	17.8	29	–	458.7	58.5	101	211	–
4	Igbori	0.9	6.7	24.1	–	118	42	187.9	802	–
5	Igbori	1.1	11.2	21	–	237.2	226.2	717.5	108.6	–
1	Igbeti	0.6	3.3	16.5	–	64.6	107.4	97.1	47.2	–
2	Igbeti	0.4	1.3	37.4	–	200.1	618.7	251.6	14.3	–
3	Igbeti	1.9	4.5	19.5	–	215.3	33.1	456.3	26.4	–
4	Igbeti	0.4	1.3	53.1	–	86.5	826.8	183.3	42.3	–
5	Igbeti	3.6	6.6	19	–	329.3	96	668.9	39.9	–
6	Igbeti	0.4	1.7	8.5	–	71.8	271.2	81	228.1	–
7	Igbeti	1.2	12	20.3	–	53.6	50.2	262.9	263.8	–
8	Igbeti	1.3	3.9	3.2	13.9	136.2	46.6	66.3	368.4	1055.7
9	Igbeti	1.2	4.2	11.2	13.7	104.3	170.3	58.1	173.9	504
10	Igbeti	1.3	9	9.3	14	107.4	151	52	60.4	793.3
1	Alaguntan	3.2	5.4	15.1	–	106.9	13.6	234.2	5.4	–
2	Alaguntan	0.5	1.6	20.7	–	149.2	954.5	23.1	118.5	–
3	Alaguntan	0.4	1.3	7.2	21.6	108.6	1126.1	14.9	347.9	84.6
4	Alaguntan	0.6	1.7	7.6	31.1	286.7	1375.8	25.8	322.2	60.7

VES	Location	h_1 (m)	h_2 (m)	h_3 (m)	h_4 (m)	ρ_1 (Ωm)	ρ_2 (Ωm)	ρ_3 (Ωm)	ρ_4 (Ωm)	ρ_5 (Ωm)
5	Alaguntan	1.1	2.7	10.5	–	397	419.5	48.1	10154.3	–

In Igbori and Alaguntan, the subsurface architecture shows distinct conductive and resistive contrasts. The Igbori profile features a thin topsoil (118–1,865 Ωm) overlying a lateritic to sandy clay layer (42–731 Ωm), with the principal weathered aquifer spanning 8 to 30 m (101–802 Ωm) and transitioning to a fractured basement (209–293 Ωm) at 30–50 m depths. At Alaguntan, a highly conductive clayey layer (14–48 Ωm, 1.3–5.4 m thick) overlies a well-developed weathered basement (23–348 Ωm, 7–31 m deep), where lower values correspond to intensely weathered, saturated zones. Across all locations, the deepest layers consistently exhibit high resistivity values (up to 20,382 Ωm in Tesi and 10,154 Ωm in Alaguntan), corresponding to unweathered, fresh crystalline bedrock that defines the lower groundwater boundary.

3.3 Geophysical Vulnerability Assessment and Characterization of Aquifer Protective Layer

The aquifer vulnerability assessment results for the four study areas are presented in Table 3. The Aquifer Vulnerability Index (AVI) classifies the majority of the study area under "extremely high" vulnerability, corresponding to poor subsurface protection. At Tesi, AVI values range from − 0.6 to 0.9, with all VES points classified as extremely high vulnerability. Similarly, Igbori (− 0.7 to 1.2) and Igbeti (− 0.8 to 1.1) are dominated by extremely high vulnerability, although localized variations occur. At Igbori, VES 3 exhibits moderate protective capacity, elevated hydraulic resistance (C = 15.9 days), and lower reflection coefficients, corresponding to thicker or less permeable weathered materials. In Igbeti, VES 3 and VES 7 show weak to moderate protective capacity (C = 8.1–13.7 days), but the majority of points remain highly vulnerable. At Alaguntan, only VES 1 is classified as high vulnerability with moderate protective capacity (C = 28.3 days), while the remaining points fall within the extremely high class (− 0.9 to − 0.5).

The longitudinal conductance (S) and transverse resistance (T) values quantify this vulnerability pattern. At Tesi, low conductance values (S = 0.008–0.132 Ω⁻¹) correspond to poorly developed protective layers. Locally high transverse resistance values (T = 225.28–8773.28 Ωm²) correspond to resistive basement or lateritic units rather than effective confining materials. At Igbori, conductance values vary widely (S = 0.006–0.315 Ω⁻¹), demonstrating lateral heterogeneity, with only VES 3 showing relatively improved protection associated with higher conductance. Similarly, Igbeti exhibits generally low conductance (S = 0.004–0.261 Ω⁻¹) and moderate transverse resistance (T = 358.8–1819.08 Ωm²), corresponding to limited protective capacity. At Alaguntan, the highest conductance value (S = 0.427 Ω⁻¹) corresponds to the only location with moderate protection, although transverse resistance remains moderate to high (T = 1507.37–2510.88 Ωm²).

Table 3
Protective Layer hydraulic parameters (hydraulic conductivity and resistance), Dar-Zarrouk parameters (S and T) and anisotropy

VES	Location	S (mhos)	K_1 (m/day)	K_2 (m/day)	C (days)	AVI	AVI Class.	Prot. Capa. Rating	T (Ωm^2)	λ
1	Tesi	0.042	1.60	32.99	1.9	0.3	Ext. High	Poor	6150.80	381
2	Tesi	0.041	1.30	7.64	1.6	0.2	Ext. High	Poor	2964.21	270
3	Tesi	0.008	15.09	59.14	0.2	-0.6	Ext. High	Poor	8773.28	1076
4	Tesi	0.061	0.09	13.37	4.7	0.7	Ext. High	Poor	550.88	95
5	Tesi	0.039	4.38	8.77	1.4	0.2	Ext. High	Poor	3627.27	306
6	Tesi	0.132	0.22	0.85	7.4	0.9	Ext. High	Weak	225.28	41
7	Tesi	0.032	0.64	6.42	1.7	0.2	Ext. High	Poor	452.89	119
8	Tesi	0.037	0.37	16.72	2.1	0.3	Ext. High	Poor	1889.29	226
9	Tesi	0.033	1.04	11.20	1.3	0.1	Ext. High	Poor	3690.32	335
10	Tesi	0.089	2.47	3.81	3.8	0.6	Ext. High	Poor	2073.67	153
1	Igbori	0.006	71.81	18.48	0.2	-0.7	Ext. High	Poor	2849.45	713
2	Igbori	0.010	40.41	23.45	0.3	-0.5	Ext. High	Poor	6439.98	793
3	Igbori	0.315	13.43	1.15	15.9	1.2	High	Moderate	3243.06	102
4	Igbori	0.167	2.65	0.77	9.0	1.0	Ext. High	Weak	387.60	48
5	Igbori	0.054	6.11	5.77	2.1	0.3	Ext. High	Poor	2794.36	227
1	Igbeti	0.040	1.29	2.37	1.9	0.3	Ext. High	Poor	393.18	99
2	Igbeti	0.004	4.98	19.21	0.1	-0.8	Ext. High	Poor	884.35	464
3	Igbeti	0.145	5.44	0.58	8.1	0.9	Ext. High	Weak	558.02	62

Prot. Capa. Rating: Protection Capacity Rating; Ext. High: Extremely High

VES	Location	S (mhos)	K_1 (m/day)	K_2 (m/day)	C (days)	AVI	AVI Class.	Prot. Capa. Rating	T (Ωm²)	λ
4	Igbeti	0.006	1.83	27.16	0.3	-0.6	Ext. High	Poor	1109.44	423
5	Igbeti	0.080	9.04	2.07	3.6	0.6	Ext. High	Poor	1819.08	151
6	Igbeti	0.012	1.46	7.17	0.5	-0.3	Ext. High	Poor	489.76	203
7	Igbeti	0.261	1.03	0.95	13.7	1.1	High	Moderate	666.72	51
8	Igbeti	0.093	3.15	0.87	4.9	0.7	Ext. High	Poor	358.80	62
9	Igbeti	0.036	2.29	4.11	1.5	0.2	Ext. High	Poor	840.42	152
10	Igbeti	0.072	2.37	3.56	3.1	0.5	Ext. High	Poor	1498.62	145
1	Alaguntan	0.427	2.36	0.20	28.3	1.5	High	Moderate	415.52	31
2	Alaguntan	0.005	3.51	32.25	0.2	-0.7	Ext. High	Poor	1601.80	564
3	Alaguntan	0.005	2.40	39.29	0.2	-0.7	Ext. High	Poor	1507.37	558
4	Alaguntan	0.003	7.66	49.92	0.1	-0.9	Ext. High	Poor	2510.88	869
5	Alaguntan	0.009	11.30	12.07	0.3	-0.5	Ext. High	Poor	1569.35	413

Prot. Capa. Rating: Protection Capacity Rating; Ext. High: Extremely High

3.4 Meso-Scale Mineralogical Controls on Geophysical Resistivity (XRD)

Quantitative mineralogical analysis using X-ray diffraction (XRD) full pattern summation revealed distinct mineral assemblages across the four rock samples collected from the Tesi, Igbeti, and Alaguntan study areas (Fig. 5). Following the classification scheme established in recent petrophysical studies, minerals were categorized as major (> 50%), secondary (10–30%), and minor/trace (< 10%) phases to evaluate their respective contributions to the bulk resistivity of the basement complex (Table 4).

Sample TSRK1 (Tesi) is quartz-rich (62.63%) with chlorite (29.14%) and muscovite (8.23%) as secondary phases, consistent with the higher resistivity values observed in this area. Sample TSRK2 (Tesi) is characterized by plagioclase (64.38%) with quartz (25.24%), amphibole (6.09%), and K-feldspar (4.29%), reflecting the intermediate resistivity values measured in this location. Sample IRK1 (Igbeti) contains plagioclase as the principal phase (49.73%), accompanied by K-feldspar (22.36%), quartz (19.89%), and amphibole (8.02%). Sample ARK1 (Alaguntan) is dominated by dolomite (70.74%), a carbonate mineral that contributes to lower resistivity values, with subordinate amphibole (22.34%) and minor calcite (6.91%).

Table 4
Quantitative phase analysis (weight %) of rock samples from Tesi, Igbeti, and Alaguntan determined by X-ray diffraction (XRD) full pattern summation.

Sample ID	Location	Mineral Phase	Weight Percent (wt.%)	Abundance Classification
TSRK1	Tesi	Quartz	62.63	Major
		Chlorite	29.14	Secondary
		Muscovite	8.23	Minor
TSRK2	Tesi	Plagioclase	64.38	Major
		Quartz	25.24	Secondary
		Amphibole	6.09	Minor
		K-feldspar	4.29	Trace
IRK1	Igbeti	Plagioclase	49.73	Major (Principal)
		K-feldspar	22.36	Secondary
		Quartz	19.89	Secondary
		Amphibole	8.02	Minor
ARK1	Alaguntan	Dolomite	70.74	Major
		Amphibole	22.34	Secondary
		Calcite	6.91	Minor

3.5 Micro-scale morphological and elemental analysis (SEM-EDS)

The SEM micrographs reveal distinct morphological features across the samples (Fig. 6). Samples TSRK1 and TSRK2 consist primarily of discrete, angular to sub-angular particles (Fig. 6a, d). At higher magnifications, these grains exhibit relatively smooth to moderately textured surfaces (Fig. 6b, e). In contrast, sample IRK1 displays aggregates of blocky and platy particles with noticeably rougher and more complex surface textures (Fig. 6g, h). Sample ARK1 is characterized by large, massive, blocky grains with distinct fracture planes and relatively smooth, dense surfaces (Fig. 6j, k).

The EDS point analyses provide the average elemental composition of these morphological features, revealing three distinct geochemical profiles (Table 5). Samples TSRK1 and TSRK2 are predominantly composed of Oxygen (54.21–57.85 wt%) and Silicon (32.99–36.02 wt%). These samples exhibit negligible concentrations of Aluminium, Calcium, Magnesium, Sodium, and Potassium (all < 0.35 wt%), alongside elevated Carbon levels (5.26–5.53 wt%). Sample IRK1 also shows high Oxygen (49.01 wt%) and Silicon (27.17 wt%) content, but is distinguished by significantly higher concentrations of Aluminium (10.20 wt%), Sodium (5.62 wt%), Calcium (3.30 wt%), and Iron (0.73 wt%) compared to the TSRK samples. Its Carbon content is comparatively lower (1.39 wt%). Sample ARK1 presents a fundamentally different elemental signature. It is dominated by Oxygen (56.95 wt%), Calcium (25.04 wt%), and Magnesium (11.96 wt%). Notably, Silicon (1.17 wt%) and Aluminium (0.00 wt%) are virtually absent in this sample. The Carbon content in ARK1 is moderate (3.21 wt%). The distinct elemental peaks

observed in the EDS spectra (Fig. 6c, f, i, l) directly corroborate the morphological variations seen in the SEM micrographs, confirming the presence of chemically distinct mineral phases across the analyzed samples.

Table 5
Comparative average elemental composition (wt%) of the analyzed rock/soil samples determined by SEM-EDX point analyses.

Element	TSRK1 (n = 4)	TSRK2 (n = 5)	IRK1 (n = 4)	ARK1 (n = 6)
Oxygen (O)	57.85 ± 1.49	54.21 ± 1.18	49.01 ± 3.18	56.95 ± 4.61
Silicon (Si)	32.99 ± 4.21	36.02 ± 8.85	27.17 ± 1.11	1.17 ± 2.86
Aluminium (Al)	1.10 ± 1.09	1.13 ± 1.24	10.20 ± 2.38	0.00 ± 0.00
Calcium (Ca)	0.01 ± 0.01	0.01 ± 0.01	3.30 ± 0.75	25.04 ± 5.80
Magnesium (Mg)	0.01 ± 0.01	0.03 ± 0.03	0.04 ± 0.08	11.96 ± 2.26
Sodium (Na)	0.01 ± 0.01	0.31 ± 0.24	5.62 ± 1.15	0.00 ± 0.00
Iron (Fe)	0.98 ± 1.68	0.06 ± 0.10	0.73 ± 1.10	0.04 ± 0.04
Potassium (K)	0.00 ± 0.00	0.00 ± 0.01	0.26 ± 0.25	0.00 ± 0.01
Carbon (C)*	5.26 ± 2.15	5.53 ± 4.85	1.39 ± 1.95	3.21 ± 3.02
Manganese (Mn)	0.00 ± 0.00	0.02 ± 0.03	0.02 ± 0.01	0.00 ± 0.00
Phosphorus (P)	0.00 ± 0.00	0.00 ± 0.01	0.00 ± 0.00	0.00 ± 0.00

Note: "n" is the number of SEM-EDX point analyses averaged per sample. Au and Pd were excluded as coating artifacts. Carbon (C) may include minor tape contributions, though elevated TSRK1 and TSRK2 levels indicate intrinsic organic matter.

4 Discussion

The curve type distributions observed in this study, particularly the predominance of H- and K-type curves at Igbeti and Alaguntan, find parallels in several regional studies. Adabanija and Ajibade [31] similarly reported H-type curves as dominant in Ogbomoso North, while Akinseye et al. [32] noted H-type curves accounting for 69% of soundings in Akure. These curve types typically indicate conductive intermediate layers that, while potentially water-bearing, often correspond to zones of high vulnerability when overlying protective layers are thin or permeable. The high diversity of curve types at Igbori (QHK, QH, OH, BA, and HA), with each type represented only once, suggests particularly complex subsurface heterogeneity, comparable to the diverse curve patterns reported by Falowo et al. [33] in Ose and Owo. It is hypothesized that this extreme heterogeneity at Igbori is not solely a product of natural geological variation but is significantly exacerbated by localized mining-induced micro-fracturing and unengineered waste dumping, which disrupt natural stratigraphic continuity. This interpretation aligns with observations from other Nigerian mining districts, where artisanal and small-scale mining activities create subsurface voids, fractures, and altered resistivity signatures that markedly modify natural geoelectric responses [34–36].

The Aquifer Vulnerability Index (AVI) results indicate that aquifer systems across the study area are highly susceptible to surface-derived contamination. These findings are consistent with reports of high aquifer vulnerability in basement terrains such as Ita-Ogbolu [37], where AVI values indicated extremely vulnerable

conditions linked to limited vadose-zone thickness and low longitudinal conductance, and parts of Ilorin [38]. Comparatively, the conductance values obtained in this study (S = 0.004–0.427 mhos) fall within the lower range reported across southwestern Nigeria, reinforcing the conclusion that weak to poor protective capacity is a widespread regional hydrogeological challenge linked to limited overburden development and low clay content [37, 38]. A strong positive association can be inferred between the thin topsoil/overburden thicknesses (0.3–3.6 m) observed in the geoelectric cross-sections and the extremely low longitudinal conductance values. This relationship indicates that the physical thickness of the weathered layer is the primary limiting factor for natural attenuation capacity, a pattern widely documented in Nigerian basement-complex and related terrains where thin vadose zones result in weak protective capacity and elevated risk of rapid contaminant breakthrough [39, 40].

These geophysical vulnerability patterns are directly explained by the bulk mineralogical framework established through XRD analysis. The carbonate-rich sample (ARK1) corresponds to the lowest resistivity values (249–3,889 Ωm) observed in the Alaguntan profile, while the quartz-rich sample (TSRK1) aligns with the significantly higher resistivity values (up to 20,382 Ωm) measured in Tesi. The dominance of quartz, plagioclase, and K-feldspar in the Tesi and Igbeti samples aligns with established mineralogical baselines for the Nigerian Basement Complex [41], while the presence of secondary phyllosilicates (chlorite, muscovite) reflects progressive weathering [42, 43]. Crucially, this mineralogy dictates the aquifer protective capacity. Primary silicates like quartz are highly stable and electrically resistive, whereas secondary minerals and carbonates possess higher cation exchange capacities (CEC) and greater specific surface areas, enhancing both attenuation potential and electrical conductivity [44]. Beyond electrical properties, the mineralogical contrast carries important implications for geochemical buffering. The high dolomite content (70.74%) in ARK1 is inferred to confer substantial Acid Neutralizing Capacity (ANC), enabling carbonate dissolution to mitigate the effects of acidic mine drainage (AMD) [45, 46]. Conversely, the quartz-dominated TSRK1 lacks meaningful buffering capacity. Consequently, acidic leachates infiltrating the Tesi area are unlikely to be neutralized, facilitating the rapid mobilization of heavy metals (e.g., Pb, Zn, Cd) from mine tailings into groundwater. This contrast underscores that aquifer vulnerability is controlled not only by physical permeability but also by the chemical resilience of the aquifer matrix.

Building upon this meso-scale understanding, the SEM-EDS micrographs and elemental analyses reveal the micro-morphological mechanisms governing rock-fluid interactions. The quartz-dominated composition of the TSRK samples (Si: 32.99–36.02 wt%, negligible Al) contrasts sharply with the aluminosilicate-rich IRK1 (Al: 10.20 wt%) and the carbonate-dominated ARK1 (Ca: 25.04 wt%, Mg: 11.96 wt%). The Al/Si atomic ratio derived from the EDS data serves as a reliable proxy for the degree of chemical weathering. Near-zero Al relative to Si in the TSRK samples indicates advanced desilication and preferential feldspar leaching, leaving behind a residual framework of highly resistive, porous quartz grains [47, 48]. This intense leaching is inferred to generate secondary micro-porosity within the rock matrix; although not always resolvable at the macro-scale, such micro-pores can substantially enhance effective permeability and thereby accelerate advective contaminant transport [49].

While elevated Si and O concentrations align with weathered basement terrains [50], the negligible Al in the TSRK samples indicates advanced feldspar leaching, leaving behind resistive quartz grains that correspond to the high-resistivity zones measured in Tesi. Conversely, the blocky, platy morphologies in IRK1, coupled with elevated Al and Na, suggest intermediate weathering stages where primary feldspars coexist with secondary clays. Furthermore, a distinct morphological contrast is observed: the highly angular, sharp-edged particles in the TSRK samples are consistent with a dominance of physical/mechanical weathering, likely accelerated by heavy machinery and blasting activities in the marble quarries. In contrast, the more rounded, blocky aggregates in IRK1 point to prolonged chemical weathering under humid tropical conditions. This morphological distinction aligns

with established SEM observations that mechanical fragmentation or crushing produces angular quartz fragments with sharp edges and high relief, whereas chemically altered zones develop rounded outlines and platy clay morphologies [51, 52].

This micro-scale heterogeneity validates the macro-scale geophysical interpretations: the uniformly poor aquifer protective capacity (S = 0.004–0.427 mhos) across the study area is fundamentally driven by the dominance of resistive, unweathered silicates and the absence of thick, conductive clay layers. This mineralogical deficiency directly translates to the high vertical hydraulic conductivity values calculated for the overburden, as the lack of fine-grained, high-cation-exchange-capacity (CEC) matrices fails to physically impede vertical fluid percolation. Unlike alluvial formations with substantial organic matter and clay content that provide natural protection through electrostatic adsorption and ion exchange [53], the fractured marble aquifers of Igbeti are characterized by rapid, channelized flow through preferential pathways with limited geochemical buffering capacity. Consequently, the travel time for surface-derived contaminants to reach the water table is drastically reduced. Without sufficient reactive mineral surfaces to retard or attenuate migrating pollutants, heavy metals and acidic leachates move conservatively through the interconnected fracture networks. This establishes a critical paradigm for the Igbeti mining district: in these silicate-dominated zones, the natural protective capacity is functionally absent, meaning that any unengineered tailings discharge will result in immediate, far-reaching, and largely irreversible groundwater contamination.

Ultimately, integrating these three scales allows for the formulation of a unified conceptual model of contaminant transport in the Igbeti mining district. The VES data maps the macro-scale physical architecture, identifying the thin, highly permeable pathways. The XRD data defines the meso-scale geochemical reactivity, revealing a lack of widespread clay/CEC buffers and localized carbonate neutralization zones. Finally, the SEM-EDS data confirms the micro-scale mechanisms, demonstrating that mechanical crushing and intense chemical leaching have created a highly porous, angular quartz matrix largely devoid of protective secondary minerals. Together, these findings demonstrate that the extremely high vulnerability of the study area arises primarily from the intrinsic lithological and mineralogical properties of the basement complex, which promote rapid, largely unattenuated contaminant migration through fractured, clay-deficient, and chemically reactive media.

5 Conclusion

In conclusion, this study successfully developed a multi-scale conceptual model of groundwater vulnerability in the Igbeti marble mining area by integrating macro-scale geophysics with meso- and micro-scale mineralogical analyses. The Vertical Electrical Sounding (VES) and Aquifer Vulnerability Index (AVI) results uniformly classified the study area as having extremely high vulnerability and poor protective capacity, characterized by low longitudinal conductance values (S = 0.004–0.427 mhos). Ground-truthing these geophysical anomalies with XRD and SEM-EDS revealed that this vulnerability is not merely a product of anthropogenic mining activities, but is fundamentally rooted in the intrinsic lithological and mineralogical properties of the fractured basement complex. The dominance of highly resistive, unweathered quartz and feldspar, coupled with advanced chemical leaching and a distinct lack of protective, high-CEC clay layers, creates a highly permeable overburden with minimal natural attenuation capacity. By resolving the non-uniqueness of geophysical interpretations through mineralogical and micro-morphological evidence, this research confirms that the fractured carbonate and silicate aquifers of Igbeti offer negligible resistance to the rapid infiltration and channelized transport of mining leachates, posing a severe and immediate threat to regional groundwater quality.

Based on the severe hydrogeological vulnerability established in this study, several critical interventions are recommended to mitigate groundwater contamination in the Igbeti mining district. First, regulatory agencies must enforce strict, science-based buffer zones around active and abandoned marble quarries, prohibiting the placement of unengineered tailings dumps and waste materials within these high-risk infiltration zones. Mining operators should be mandated to implement engineered, impermeable leachate collection systems and lined tailings dams to prevent the direct percolation of acidic and heavy-metal-laden runoff into the fractured bedrock. Furthermore, a continuous, long-term hydrogeochemical monitoring network should be established to track the spatial and temporal migration of mining-derived contaminants in shallow aquifers, particularly during peak rainfall seasons when infiltration rates are highest. For future research, it is recommended to integrate 2D/3D Electrical Resistivity Tomography (ERT) with isotopic tracing techniques to definitively fingerprint and delineate the precise spatial extent of contaminant plumes migrating through these complex, fractured media.

Declarations

Acknowledgements

Not applicable.

Author Contributions

Ayodele Christianah Adeboye: Writing – Original Draft, Investigation, Methodology, Formal Analysis, Data Curation; Oladele Ajiboro Omotoso: Conceptualization, Writing – Review & Editing, Supervision, Resources, Methodology; Omolayo Ajoke Omorinoye: Writing – Review & Editing, Supervision, Methodology. This research forms part of the PhD work of Ayodele Christianah Adeboye at the University of Ilorin. All authors have read and agreed to the published version of the manuscript.

Funding

No funds, grants, or other support was received.

Data availability

The authors declare that all data used in this study are original and are provided directly in this manuscript.

Ethics approval and consent to participate

Not applicable.

Consent for publication

Not applicable.

Clinical trial number

Not applicable.

Competing interests

The authors declare no competing interests.

References

1. Egbueri JC, Agbasi JC, Ayejoto DA, Khan MI, Khan MYA. Extent of anthropogenic influence on groundwater quality and human health-related risks: An integrated assessment based on selected physicochemical characteristics. Geocarto Int. 2023;38:2210100. https://doi.org/10.1080/10106049.2023.2210100.
2. Balwant P, Pujari PR, Dhyani S, Bramhanwade K, Jyothis V. Geophysical Methods for Assessing Microbial Processes in Soil: A Critical Review. Indian J Pure Appl Sci. 2022;60:707–15. https://doi.org/10.56042/ijpap.v60i8.63548.
3. Edokpayi JN, Rogawski ET, Kahler DM, Hill CL, Reynolds C, Nyathi E, et al. Challenges to Sustainable Safe Drinking Water: A Case Study of Water Quality and Use across Seasons in Rural Communities in Limpopo Province, South Africa. Water. 2018;10:159. https://doi.org/10.3390/w10020159.
4. Wiederhold H, Kallesøe AJ, Kirsch R, Mecking R, Pechnig R, Skowronek F. Geophysical methods help to assess potential groundwater extraction sites. Grundwasser. 2021;26:367–78. https://doi.org/10.1007/s00767-021-00495-x.
5. Olagunju D. Igbeti: From marble site to forest reserve? [Internet]. 2016. https://tribuneonlineng.com/igbeti-marble-site-forest-reserve
6. Alamu AO. The need for political and environmental appraisal of Igbeti marble and its implications for socioeconomic development in Oyo State, Nigeria. Int J Novel Res Humanit Social Sci Manage. 2018;1.
7. Afolayan OS. Impact of marble mining on selected soil properties in Igbeti, Oke-Ogun area of Oyo State, Nigeria. 2021.
8. Aina A, Emofurieta WO. The use of very low frequency electromagnetic method for non-conductive resource evaluation and geological mapping. J Afr Earth Sci (and Middle East). 1991;12:609–16. https://doi.org/10.1016/0899-5362(91)90023-r.
9. Emofurieta W, Ekuajemi V. Lime Products and Economic Aspects of Igbetti, Ososo and Jakura Marble Deposits in Southwest Nigeria. J Min Geol. 1995;31:127–37.
10. Nigerian Geological Survey Agency. Geological Maps [Internet]. 2020. https://ngsa.gov.ng/geological-maps/
11. Binley A, Hubbard SS, Huisman JA, Revil A, Robinson DA, Singha K, et al. The emergence of hydrogeophysics for improved understanding of subsurface processes over multiple scales. Water Resour Res. 2015;51:3837–66.
12. Day-Lewis FD, Slater LD, Robinson J, Johnson CD, Terry N, Werkema D. An overview of geophysical technologies appropriate for characterization and monitoring at fractured-rock sites. J Environ Manage. 2017;204:709–20. https://doi.org/10.1016/j.jenvman.2017.04.033.
13. Aizebeokhai AP, Oyeyemi DK, Joel SE. Groundwater potential assessment in a sedimentary terrain, southwestern Nigeria. Arab J Geoscience. 2016;9:496.
14. Yin C. Geoelectrical inversion for a one-dimensional anisotropic model and inherent non-uniqueness. Geophys J Int. 2000;140:11–23.
15. Rezaee R. Quantifying natural hydrogen generation rates and volumetric potential in onshore serpentinization. Geosciences. 2025;15:112.
16. Revil A, Wu Y, Karaoulis M, Hubbard SS, Watson DB, Eppehimer JD. Geochemical and geophysical responses during the infiltration of fresh water into the contaminated saprolite of the Oak Ridge Integrated Field Research Challenge site, Tennessee. Water Resour Res. 2013;49:4952–70.

17. Watson DB, Doll WE, Gamey TJ, Sheehan RJ, Jardine PM. Plume and lithologic profiling with surface resistivity and seismic tomography. Groundwater. 2005;43:169–77.
18. Park SG, Shin SW, Lee DK, Kim CR, Son JS. Relationship between electrical resistivity and physical properties of rocks. Near Surface Geoscience 2016-First Conference on Geophysics for Mineral Exploration and Mining. European Association of Geoscientists & Engineers; 2016. pp. 1–5.
19. Li H, Li H, Wang K, Liu C. Effect of rock composition microstructure and pore characteristics on its rock mechanics properties. Int J Min Sci Technol. 2018;28:303–8. https://doi.org/10.1016/j.ijmst.2017.12.008.
20. Rahaman MA, Emofurieta WO, Caen-Vachette M. The potassic-granites of the Igbeti area: further evidence of the polycyclic evolution of the Pan-African belt in southwestern Nigeria. Precambrian Res. 1983;22:75–92. https://doi.org/10.1016/0301-9268(83)90059-1.
21. Loke MH. Tutorial: 2-D and 3-D electrical imaging surveys. Geotomo Software; 2001.
22. Jung-Ho K. Dippro for Windows, Dipro TM version 4.0: Processing and interpretation software for dipole-dipole electrical resistivity data. Kigam; 2001.
23. Adepelumi AA, Ako BD, Ajayi TR, Olorunfemi AO, Awoyemi MO, Falebita DE. Integrated geophysical mapping of the Ifewara transcurrent fault system, Nigeria. J Afr Earth Sc. 2008;52:161–6.
24. Altomare A, Cuocci C, Giacovazzo C, Moliterni A, Rizzi R. QUALX: a computer program for qualitative analysis using powder diffraction data. J Appl Crystallogr. 2008;41:815–7.
25. Butler BM, Hillier S, powdR. An R package for quantitative mineralogy using full pattern summation of X-ray powder diffraction data. Comput Geosci. 2021;147:104662.
26. Eberl DD. User guide to RockJock-A program for determining quantitative mineralogy from X-ray diffraction data. US Geological Survey; 2003. pp. 2003–78. Report No.
27. Kosinski WK, Kelly WE. Geoelectric soundings for predicting aquifer properties. Groundwater. 1981;19:163–71.
28. Koefoed O. Resistivity sounding on an earth model containing transition layers with linear change of resistivity with depth. Geophys Prospect. 1979;27:862–8.
29. Maillet R. The fundamental equations of electrical prospecting. Geophysics. 1947;12:529–56.
30. Stempvoort DV, Ewert L, Wassenaar L. Aquifer vulnerability index: a GIS-compatible method for groundwater vulnerability mapping. Can Water Resour J. 1993;18:25–37.
31. Adabanija MA, Ajibade RA. Investigating groundwater corrosion and overburden protective capacity in a low latitude crystalline basement complex of southwestern Nigeria. NRIAG J Astron Geophys. 2020;9:245–59.
32. Akinseye VO, Osisanya WO, Eyankware MO, Korode IA, Ibitoye AT. Application of second-order geoelectric indices in determination of groundwater vulnerability in hard rock terrain in SW. Nigeria Sustainable Water Resour Manage. 2023;9:169.
33. Falowo OO, Akindureni Y, Ojo O. Groundwater assessment and its intrinsic vulnerability studies using aquifer vulnerability index and GOD methods. Int J Energy Environ Sci. 2017;2:103–16.
34. Idogbe EA, Ahmed AL, Lawal KM, Ahmed BM, Isah MM. 2D electrical resistivity imaging of mine workings at Odagbo, North Central Nigeria. FUDMA J Sci. 2019;3:210–5.
35. Davou HD, Odeuwmi SC, Akanbi ES. Subsurface cavity detection using 2D electrical resistivity tomography at some mining sites in Jos, northcentral Nigeria. FUPRE J Sci Industrial Res. 2024;8:208–18.

36. Yusuf SN, Ejepu JS, Ogunmola JK, Yohanna OM, Wakili WM. The use of electrical resistivity tomography method to resolve land boundary disputes in mining areas. Scientia Africana. 2024;23:259–72.
37. Falowo OO. Modeling of hydrogeological parameters and aquifer vulnerability assessment for groundwater resource potentiality prediction at Ita Ogbolu, Southwestern Nigeria. Model Earth Syst Environ. 2023;9:749–69.
38. Abubakar HO, Adebisi WA, Folorunso IO, Adeoye TO, Olatunji S, Odangbe CO. Aquifer Vulnerability Index Model for Vulnerability Assessment: A Case Study of Irewolede Estate in Ilorin, North-Central Nigeria. J Earth Space Phys. 2025;50.
39. Aweto KE, Ohwoghere-Asuma O, Omeru T. A comparative aquifer vulnerability study of the Quaternary Sombreiro-Warri Deltaic Plain deposits, western Niger Delta, Nigeria. 2023.
40. Ayua KJ, Alimi GI, Bamigbaiye FF, Akbar AJ. Synthesizing vulnerability indices within a diverse lithological context: Corollaries for groundwater quality assurance and surface layer corrosiveness of Lokoja Geomaterials, Nigeria. Water Pract Technol. 2024;19:3744–62.
41. Hussaini SU. Hydrogeochemical investigation of groundwater quality in Zing and its environs, part of Jalingo Sheet 236NE, north-eastern Nigeria [PhD Thesis]. Federal University of Technology, Minna; 2023.
42. Gao Q, Shang Y, Hasan M, Jin W, Yang P. Evaluation of a Weathered Rock Aquifer Using ERT Method in South Guangdong, China. Water. 2018;10:293. https://doi.org/10.3390/w10030293.
43. Ojo OA, Oyelami CA, Fakunle MA, Ogundana AK, Ajayi OE, Uche TE. Integrated approach to unsaturated zone characterization as it relates to burial practices and its impact on the immediate environment. Heliyon. 2022;8.
44. Otene OG, Adejumo TE, Amadi AA, Eze FE. Leachate-induced soil mineralogical alterations at the Gosa dumpsite in Abuja, Nigeria. Int J Environ Des Constr Manage. 2025.
45. Gomo M. Conceptual hydrogeochemical characteristics of a calcite and dolomite acid mine drainage neutralised circumneutral groundwater system. Water Sci. 2018;32:355–61.
46. Chai Y, Qin P, Zhang J, Wu Z, Li T, Xu W, et al. Experimental study and application of dolomite aeration oxidation filter bed for the treatment of acid mine drainage. Miner Eng. 2020;157:106560.
47. Ruxton BP. Measures of the degree of chemical weathering of rocks. J Geol. 1968;76:518–27.
48. Qiu S, Zhu Z, Yang T, Wu Y, Bai Y, Ouyang T. Chemical weathering of monsoonal eastern China: implications from major elements of topsoil. J Asian Earth Sci. 2014;81:77–90.
49. Yuan G, Cao Y, Schulz HM, Hao F, Gluyas J, Liu K, et al. A review of feldspar alteration and its geological significance in sedimentary basins: From shallow aquifers to deep hydrocarbon reservoirs. Earth Sci Rev. 2019;191:114–40.
50. Chidambaram S, Senthil Kumar G, Prasanna MV, John Peter A, Ramanthan AL, Srinivasamoorthy K. A study on the hydrogeology and hydrogeochemistry of groundwater from different depths in a coastal aquifer: Annamalai Nagar, Tamilnadu, India. Environ Geol. 2009;57:59–73.
51. Degórski M, Kowalkowski A. The use of SEM morphoscopy in researching the litho-pedogenetic environments evolution of Late Pleistocene and Holocene. Geographia Pol. 2011;84:17–38.
52. Dekhtyar Y, Kalnina R, Skrebele E, Sorokins H, Gorohovs M, Tenters F. Preliminary Assessment of Quartz Sand Properties from Latvian Coastal Beaches for Potential Filtration Applications. Materials. 2026;19:809. https://doi.org/10.3390/ma19040809.

53. Akhtar N, Syakir MI, Tweib SA, Aminuddin MIKA, Yusuff MSM, Alsabhan AH, et al. Particle size distribution and composition of soil sample analysis in a single pumping well using a scanning electron microscope coupled with an energy dispersive X-ray (SEM-EDX) and the laser diffraction method (LDM). Water. 2023;15:3109.

Figures

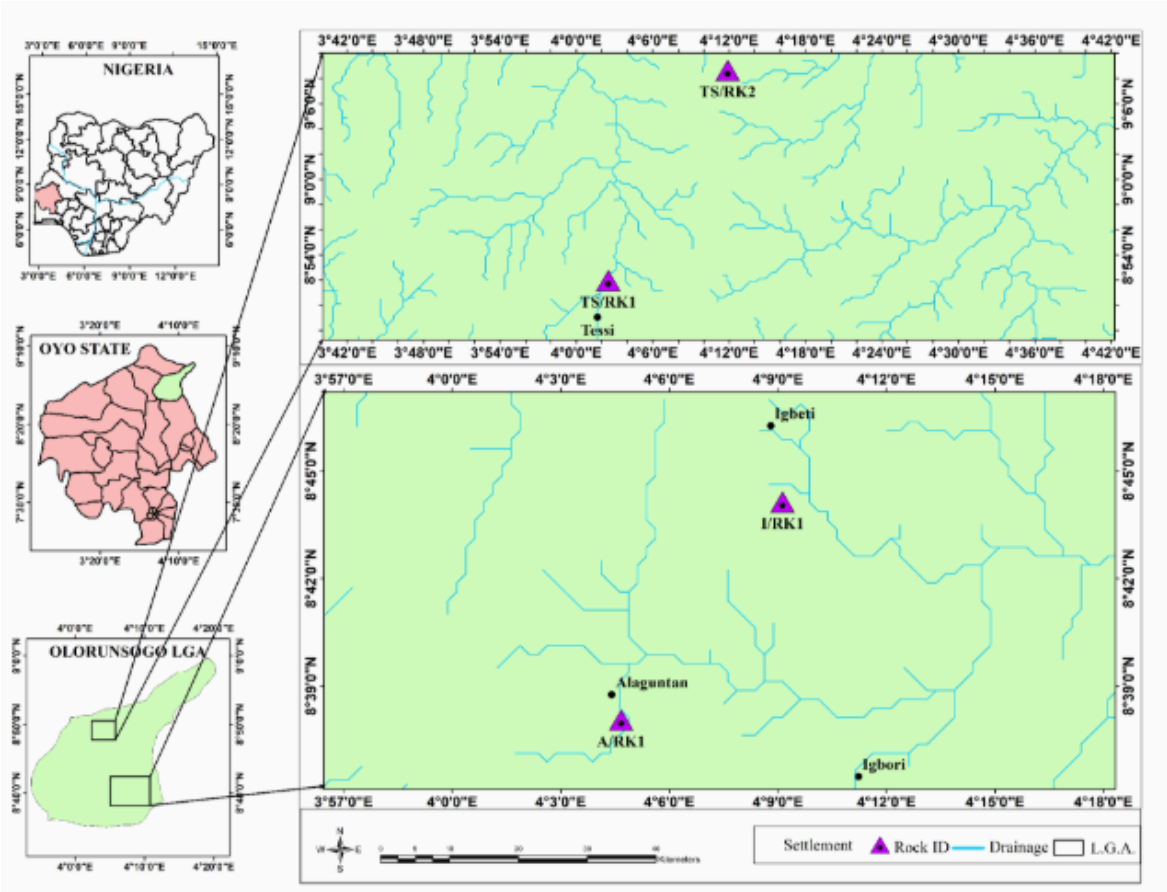


Figure 1

Sample Location Map

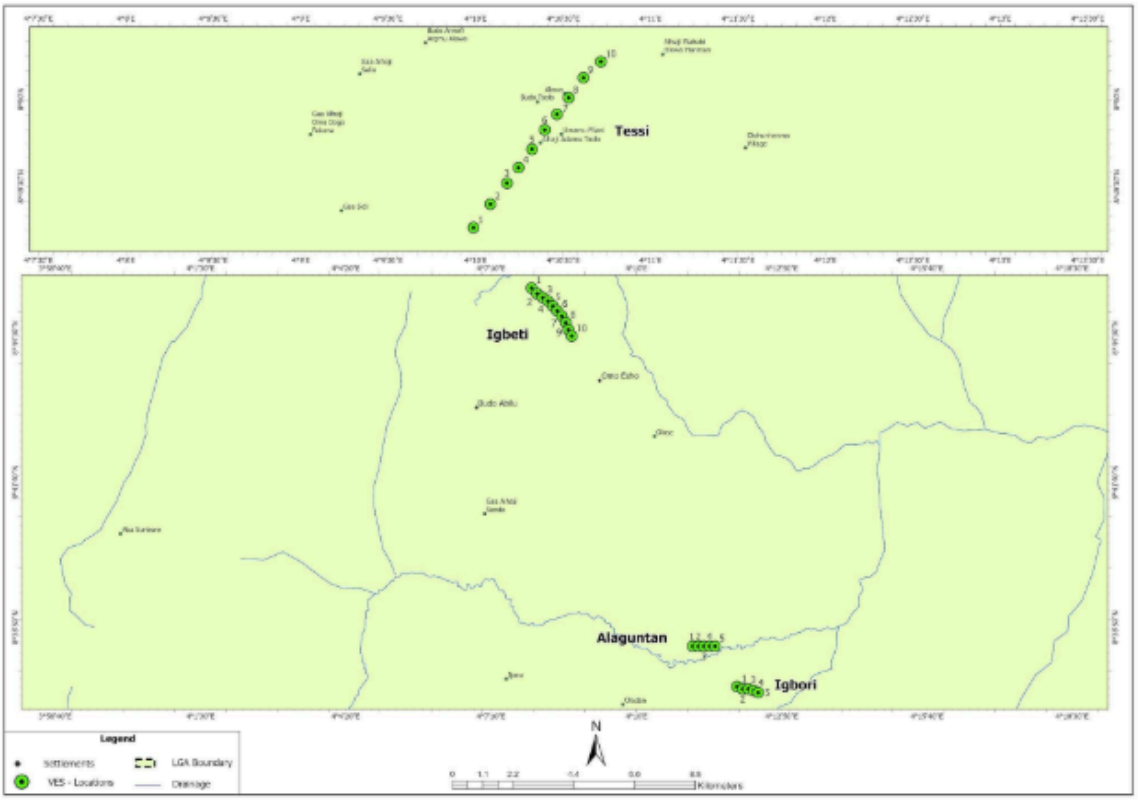


Figure 2

Map of the study Area showing the position of collinear VES points (Profiles)

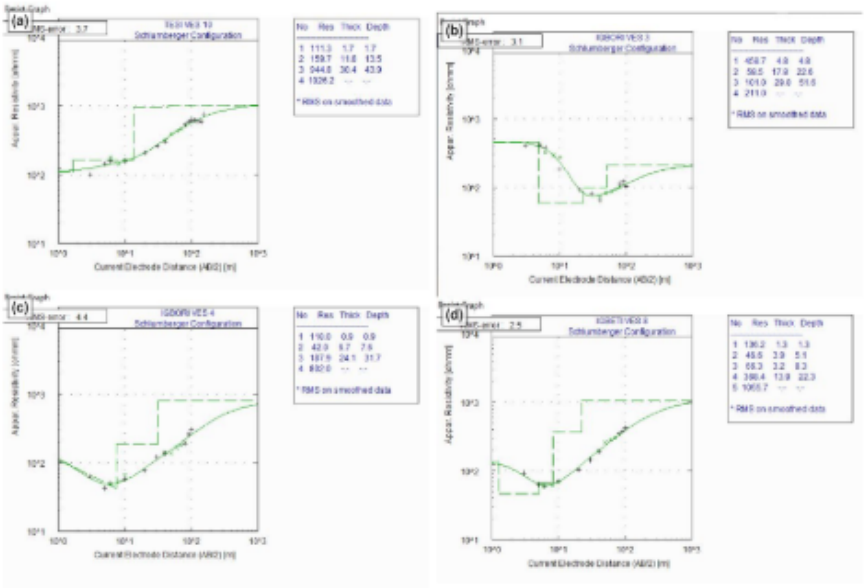


Figure 3

Representative apparent resistivity (VES) curves from the study area showing variations in subsurface layering across (a) Tesi (VES 10), (b) Igbori (VES 3), (c) Igbori (VES 4), and (d) Igbeti (VES 8).

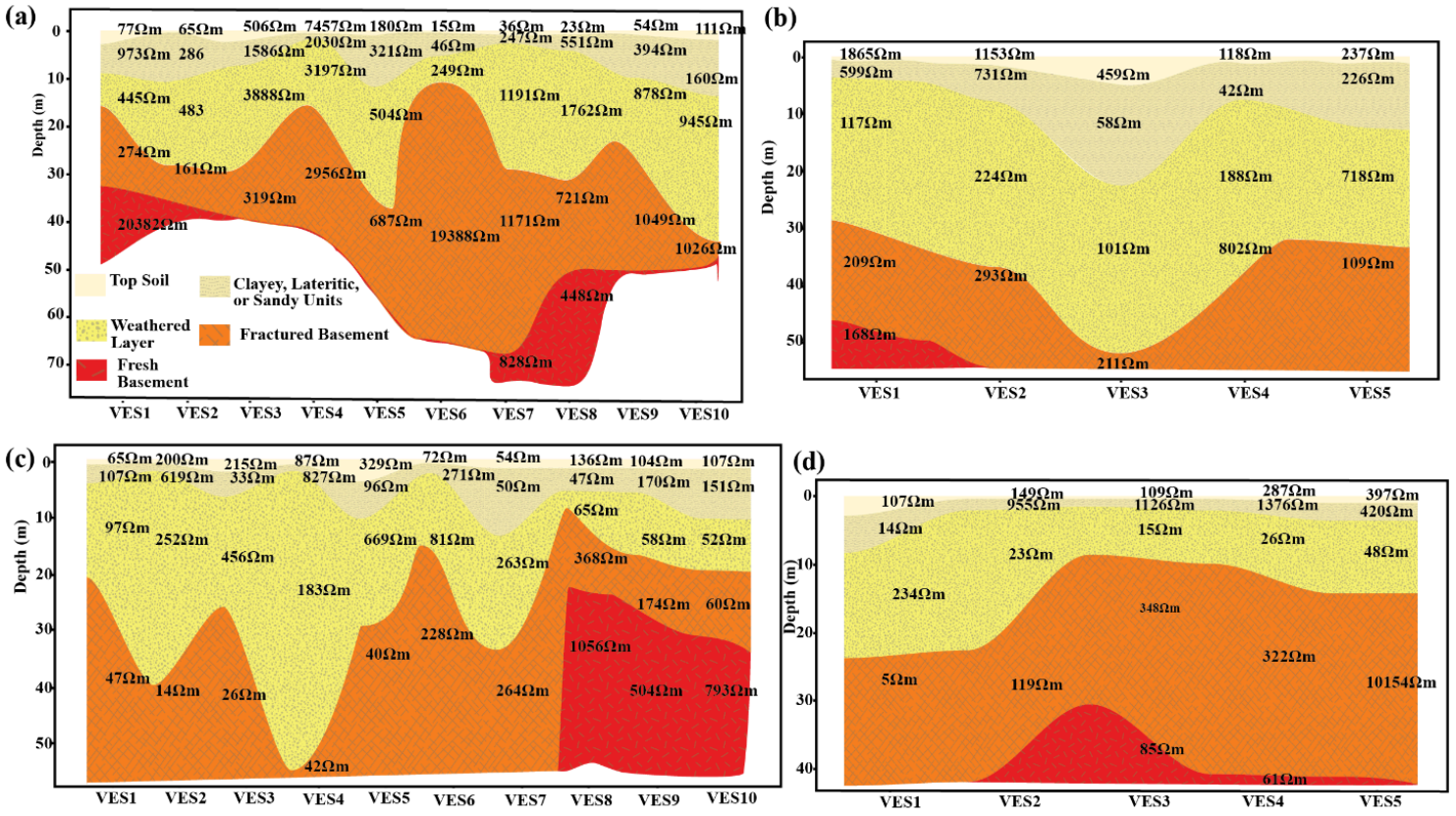


Figure 4

Geoelectric cross-sections derived from 1-D VES interpretation along the study profiles showing subsurface resistivity variation and layer geometry at (a) Tesi, (b) Igbori, (c) Igbeti, and (d) Alaguntan.

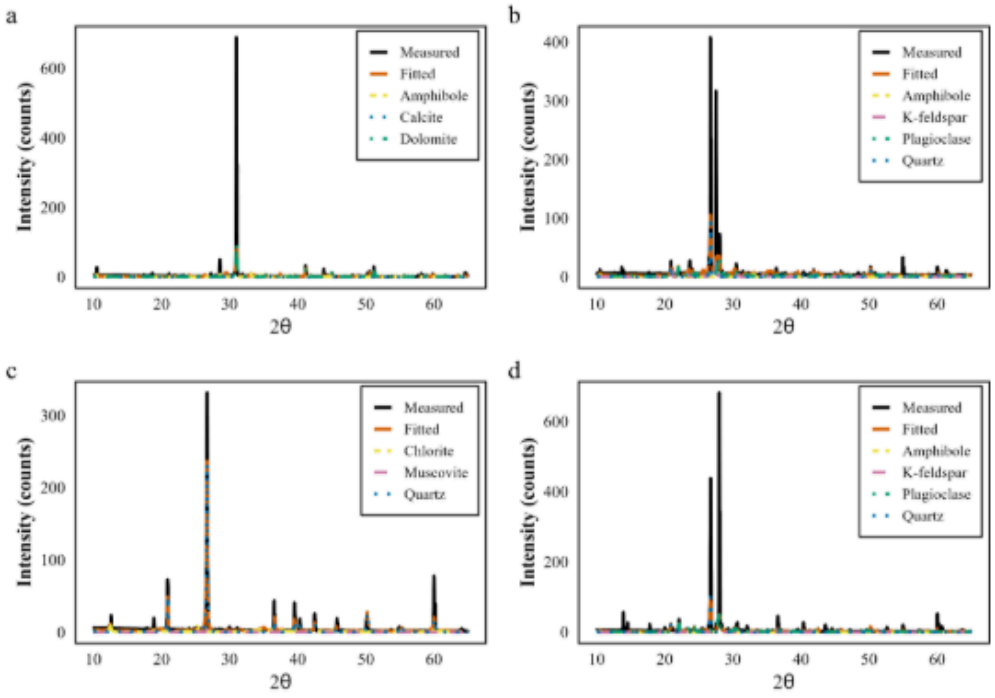


Figure 5

X-ray diffraction (XRD) full pattern summation profiles showing measured (black line) and fitted (red line) patterns with individual mineral phase contributions for samples: (a) ARK1, (b) IRK1, (c) TSRK1, and (d) TSRK2.

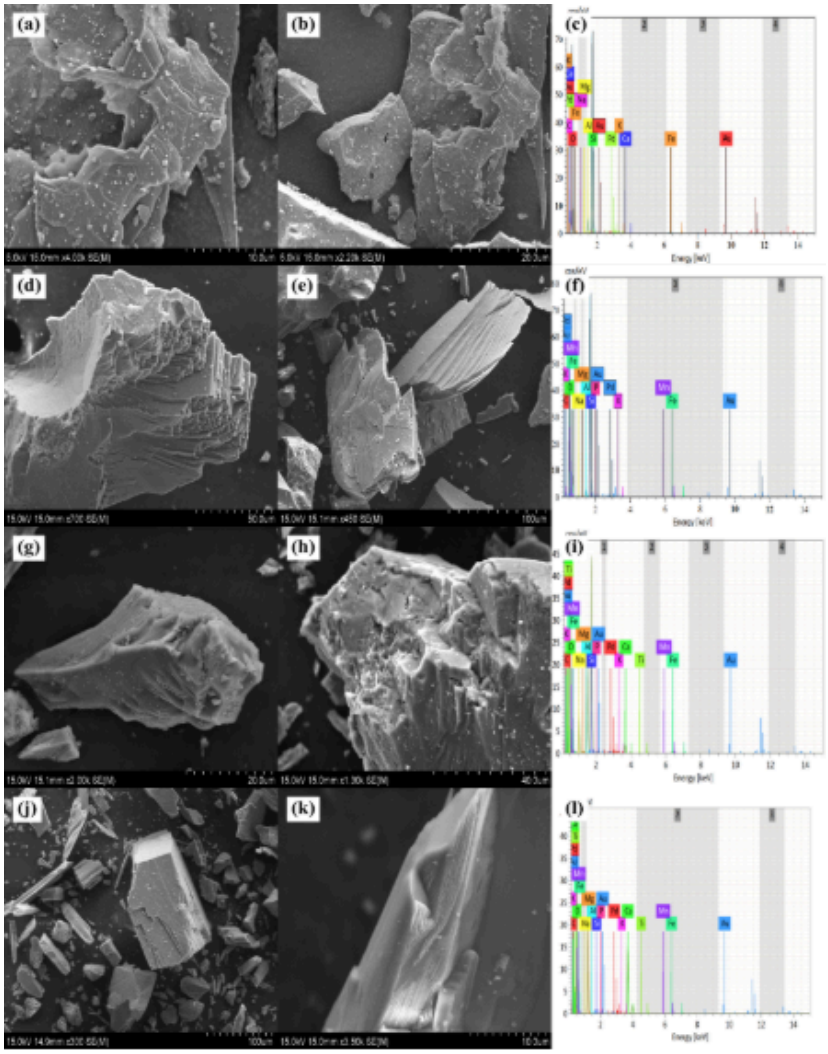


Figure 6

SEM micrographs and EDX spectra of the analyzed samples. (a–c) TSRK1 (4000×, 2200×, and Spectrum 1). (d–f) TSRK2 (700×, 450×, and Spectrum 1). (g–i) IRK1 (2000×, 1300×, and Spectrum 6). (j–l) ARK1 (300×, 3500×, and Spectrum 10). The images display distinct grain morphologies and surface textures, corroborated by the elemental composition profiles. (Au and Pd peaks are sputter-coating artifacts).